CrossMark

ORIGINAL RESEARCH PAPER

Seismic behavior of self-centering reinforced concrete wall enabled by superelastic shape memory alloy bars

Bin Wang[1,2] · Songye Zhu[1] (ORCID)

Abstract Reinforced concrete (RC) wall is a common type of structural component used in high-rise buildings to resist lateral loads induced by earthquakes. RC walls are typically designed and detailed to dissipate energy through significant inelastic responses to meet expected seismic performance under moderate-to-strong earthquakes. However, costly repair or even demolition caused by excessive residual deformation is usually inevitable. Given this deficiency, this study investigates the feasibility of utilizing superelastic shape memory alloy (SMA) bars to achieve self-centering (SC) RC walls. Under this condition, the residual deformation of SC–RC walls is reduced by superelastic SMA with large recoverable strain and remarkable fatigue properties. The mechanical properties of superelastic nickel–titanium bars and SC–RC wall design are described. A numerical SC–RC wall model is developed and validated by comparing the test results. Parametric studies of SC–RC wall systems are then conducted to investigate the effects of axial compressive load ratio, bottom slit length, and lower plateau stress factor of SMA. Results show that the proposed SC–RC walls have excellent SC ability and moderate energy dissipation capacity. The damage regions and levels of the SC–RC wall systems are also discussed.

✉ Songye Zhu
ceszhu@polyu.edu.hk

Bin Wang
btjwang@polyu.edu.hk

[1] Department of Civil and Environmental Engineering, Hong Kong Polytechnic University, Hong Kong, China

[2] State Key Laboratory of Subtropical Building Science, South China University of Technology, Guangzhou, China

🖄 Springer

1 Introduction

Reinforced concrete (RC) walls are predominant types of structural components extensively used in high-rise buildings to resist lateral loads induced by earthquakes. Modern seismic design philosophy (CEN 2004; ACI 2014) allows RC walls to experience significant inelastic response to dissipate energy at plastic hinge regions when subjected to moderate-to-strong earthquakes. Even though the target performance (e.g., collapse prevention) of RC walls can be satisfactorily achieved, such a design philosophy may result in permanent damage concentrated in selected "sacrificial" regions after earthquakes. Damaged buildings are often demolished because extremely large residual deformation makes repairs economically unviable. Figure 1 shows the post-earthquake reconnaissance of the 2010 Chile Maule earthquake and the 2011 New Zealand Christchurch earthquake, wherein parts of existing RC structures designed according to modern seismic codes were heavily damaged without collapse but demolished after the earthquakes. Consequently, approximately 60% of RC buildings after the Christchurch earthquake were demolished because of costly repair, which led to the closure of the central business district for over two years (Marquis et al. 2017). A recent study concluded that residual drift higher than 0.5% justifies a more economical rebuilding of a new structure than retrofitting the damaged structure (McCormick et al. 2008). New seismic protection concepts, such as resilience-based design (RBD) (Bruneau and Reinhorn 2007) and damage avoidance designs (DAD) (Mander and Cheng 1997; Bradley et al. 2008), emerged recently to minimize structural damage through new technologies and advanced materials.

Fig. 1 Observed damage of RC wall after earthquakes: **a** Plaza del Rio building A, 12-story, demolished after 2010 Maule earthquake (NIST 2014); **b** hotel grand chancellor, 26-story, demolished after 2011 Christchurch earthquake (Wikipedia 2017)

A common type of self-centering (SC) RC wall involves the combined use of unbonded post-tensioned (PT) tendons and supplementary energy dissipation devices to create a hybrid wall system (Holden et al. 2003; Restrepo and Rahman 2007; Smith et al. 2011). Flag-shaped hysteretic loops are the major characteristics of these hybrid systems. Rocking motions during earthquakes allow gap opening/closing at the wall bases to reduce (or even eliminate) residual deformation and wall system damage. SC behavior is realized by the restoring force provided by PT tendons and vertical load, whereas stable energy dissipation is supplemented by additional components, such as mild steel bars (Holden et al. 2003; Restrepo and Rahman 2007; Smith et al. 2011), friction dampers (Wolski et al. 2009; Guo et al. 2014; Hashemi et al. 2016), or other damping devices (Kam et al. 2010; Vasdravellis et al. 2013; Sritharan et al. 2015; Tzimas et al. 2016; Di Cesare et al. 2017). The potential superior performance of the hybrid wall system was extended to masonry (Toranzo et al. 2009) and timber walls (Iqbal et al. 2015; Kramer et al. 2016).

As an advanced metallic material, shape memory alloys (SMAs) can undergo large strains and recover their initial shape through heating (shape memory effect) or unloading (superelastic effect) (DesRoches et al. 2004). The superelasticity of SMA is appealing to the earthquake engineering research community because flag-shaped hysteresis is associated with minimal residual deformation under cyclic loading. At low strain ($\varepsilon < 1\%$), the large modulus of elasticity of the austenite phase can limit deformation under in-service load conditions. The reduced modulus of the intermediate strain plateau ($1\% < \varepsilon < 6\%$) can be used to limit the force transmitted to adjacent structural components when undergoing rather large displacements. The increased modulus of the martensite phase at large strain ($\varepsilon > 6\%$) can be used to control displacement during severe earthquakes (McCormick et al. 2007).

Superior superelastic behavior of SMA received increasing interest for seismic protection applications, including SMA braces (Zhang and Zhu 2007, 2008; Zhu and Zhang 2007, 2008; Araki et al. 2016; Qiu and Zhu 2017), SMA-based isolators and dampers (Dolce et al. 2007; Ma and Cho 2008; Shook et al. 2008; Casciati and Favavelli 2008, 2009; Ozbulut and Silwal 2016; Qian et al. 2016) and SMA-based structural connections (Speicher et al. 2011; Fang et al. 2014; Wang et al. 2017). In particular, the use of superelastic SMAs as reinforcement in concrete structures was explored recently. Youssef et al. (2008) tested RC beam–column joint reinforced with superelastic SMA bars under reversed loading. Results showed that the SMA-reinforced beam–column joint could recover most of its post-yield deformation. Saiidi et al. (2007) tested a small-scaled concrete beam with nickel–titanium (NiTi) reinforcement under half-cycle loads. The test results showed that the average residual displacement in the NiTi reinforced beams was less than one-fifth of that of the conventional steel reinforced beams. Saiidi and Wang (2006) and Saiidi et al. (2009) also conducted shake table and quasi-static tests on concrete bridge columns reinforced with SMA longitudinal reinforcement in the plastic hinge area. Their results demonstrated that SMA-reinforced columns significantly reduced residual deformation. Tazarv and Saiidi (2015) provided mechanical properties and design specifications for reinforcing superelastic NiTi. Alam et al. (2009) evaluated the seismic behavior of concrete frames reinforced with SMAs located in a highly seismic region through non-linear time-history analyses. Results show that SMA RC frames could recover most of their large inelastic deformation even after a strong earthquake. However, previous studies were mainly focused on superelastic SMA reinforcement in RC beam, column, and beam–column joint. Studies on SC–RC walls reinforced by superelastic SMA bars remain limited.

This study investigates the seismic behavior of SC–RC walls enabled by superelastic SMA bars. To reduce residual deformation, SC–RC walls utilize unbonded superelastic NiTi bars with the large recoverable strain and remarkable fatigue property arranged in the two-side boundary zones. The mechanical properties of SMA bars and the SC–RC wall design are described. An analytical SC–RC wall model is developed and validated using representative test results. Subsequently, parametric SC–RC wall studies are performed to investigate the effects of axial compressive load ratio, the length of bottom slit, and the lower plateau stress factor of SMA. The potential damage regions and levels of the SC–RC walls are also discussed.
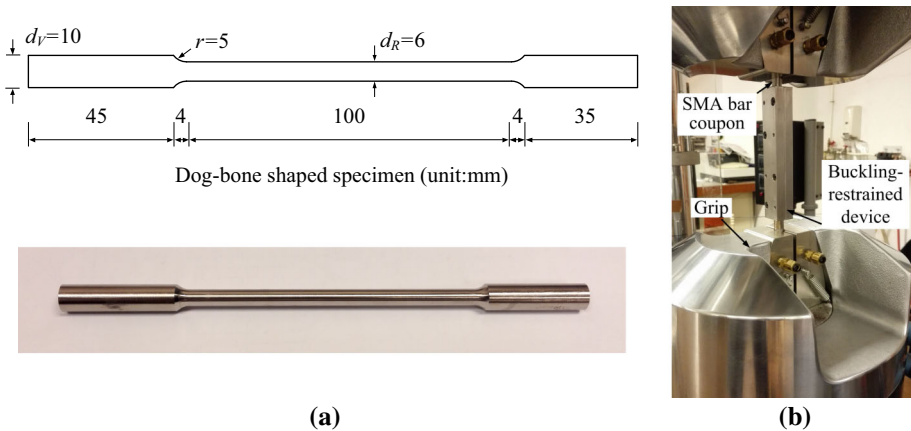
2 Cyclic test of buckling-restrained NiTi bar

The mechanical properties of SMA materials are related to phase transformation (thermal conditions). Figure 2 shows the schematic of stress–strain responses of superelastic and shape memory SMAs. The stress–strain behavior of SMA is similar to the conventional steel with fat hysteresis loop and remarkable residual strain at a temperature below the martensite finish temperature $T < M_f$; however, residual strain can be recovered through temperature increase. When temperature increases above the austenite finish temperature $T > A_f$, SMA exhibits superelastic behavior with little or no residual strain, which is caused by a stress-induced phase transformation from austenite to martensite (Graesser and Cozzarelli 1991). NiTi (also known as Nitinol) is the most commonly used SMAs because of its excellent superelastic behavior (recoverable strain up to 8%) and high fatigue performance (Zhang and Zhu 2008; Casciati et al. 2017). Superelastic NiTi bars are selected in this study because of their superior material properties.

All NiTi specimens tested in this study were hot-rolled bars and machined to the dog-bone shaped coupons. Figure 3a shows that the virgin bar diameter is $d_V = 10$ mm and the
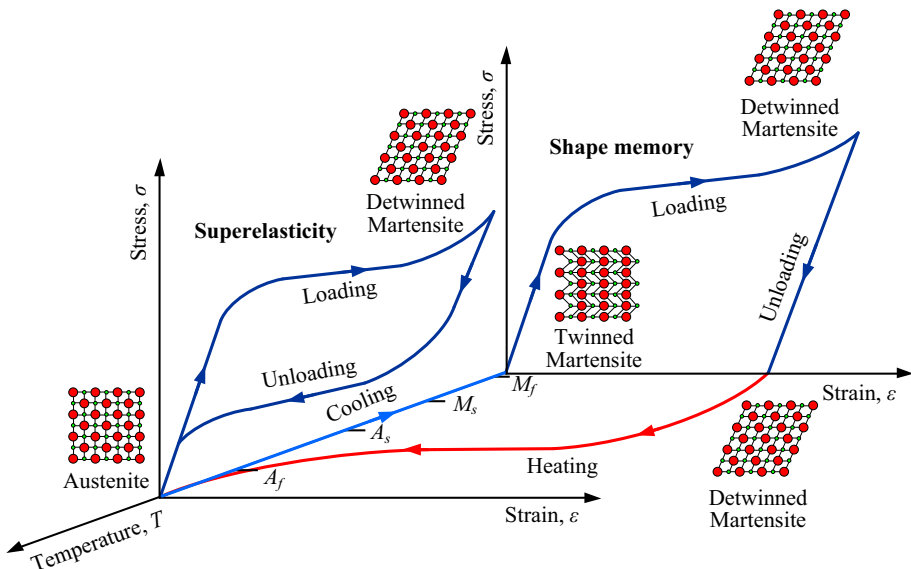
**Fig. 2** Schematic of stress–strain responses of superelastic and shape memory effects of SMAs

Fig. 3 Cyclic test of buckling-restrained NiTi bar: **a** coupon dimension and configuration; **b** MTS test

reduced diameter is $d_R = 6$ mm. The austenite finish temperature A_f is between 0 and 5 °C, which can exhibit superelastic behavior at room temperature according to the information from the material supplier. The machined specimens were heat-treated in an electrical furnace at 400 °C for 30 min and water-quenched afterward.

Figure 3b shows the cyclic tension–compression coupon tests with buckling-restrained device that were performed on an MTS machine. The loading protocol with increasing strain amplitudes was applied, namely, 0.5, 1.0, 2.0, 3.0, 4.0, 5.0, and 6.0%, with two repeated cycles at each strain amplitude. The cyclic tests were conducted at a room temperature of 23–26 °C with a constant loading strain rate of 0.0005 s^{-1}. Figure 4 shows a representative stress–strain relationship of the tested NiTi bar. Satisfactory flag-shaped hysteretic loops were obtained in multiple loading cycles without any strength degradation in tension and compression directions. The stress–strain curves under tension and compression are asymmetric, wherein compressive stress is higher than the tensile stress under the same strain. Figure 4 shows that the forward (austenite to martensite) phase transformation began at approximately 460.7 MPa and finished with apparent hardening at approximately 6% strain under tension. After 14 loading cycles, the residual strain under tension was less than 0.16% when unloading from the peak strain of 6%. By contrast, the forward phase transformation under compression began at approximately 621.3 MPa and

Fig. 4 Stress–strain relationship of superelastic SMA bar with increasing strain loading
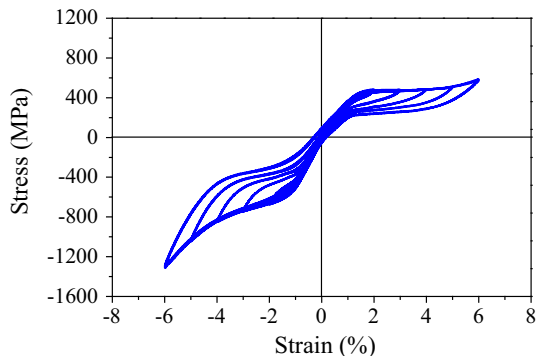
the strain hardened earlier. Residual strain was less than 0.32% after unloading from 6% strain level. To eliminate the "training" effect, which refers to the variation of the stress–strain curves in initial cycles, the SMA bars are usually cyclically preloaded until the hysteretic loops of the material stabilizes (Zhang and Zhu 2008). In this study, the hysteretic behavior of the NiTi bar was fully stabilized after nine loading cycles with 6% strain amplitude. Table 1 presents the stabilized mechanical properties of the NiTi bar and the parameters of hysteretic behavior used in subsequent numerical studies. In this study, the strain values at the start of martensite phase transformation both are equal to 1.5% in tension and compression direction, whereas the strain values at the completion of martensite phase transformation are equal to 6 and 5% in tension and compression direction, respectively.

# 3 Description and design of SC–RC wall

In this study, the representative rectangular wall RW2 (referred as RC wall hereinafter) tested by Thomsen and Wallace (2004) was selected as the reference structure. The original prototype building was designed as special structural walls that represented a typical office building located in high-seismicity area (e.g., Los Angeles). Wall height was 3660 mm and the cross-section was 1220 mm × 102 mm. The specimen with an aspect ratio of 3.0 was designed to fail in a flexural–dominant mode. Longitudinal reinforcement at the wall boundaries consisted of 8#3 ($\emptyset = 9.53$ mm) bars, whereas uniformly distributed web reinforcement consisted of two curtains of #2 ($\emptyset = 6.35$ mm) bars. The compressive strength of concrete was 42.8 MPa. The yield strengths of three reinforcement types, namely, #3, #2, and hoop, were 434, 448, and 434 MPa, respectively. A compressive load of approximately 0.07 $A_g f_c$ (378 kN) was applied at the top of the wall through load transfer assembly, where A_g was the cross-sectional area of the wall and f_c was the concrete compressive strength. More design details can be found in Thomsen and Wallace (2004).

The SC–RC wall in this study is designed with reference to the RW2 specimen. Figure 5 shows the dimensions and reinforcement details of the SC–RC wall. The geometry, material, and web reinforcement details are similar to RW2, except for the unbonded superelastic SMA bars used as the longitudinal reinforcement in two-side boundary zones, which are the expected regions of plastic hinges. The upper ends of SMA bars are connected to the conventional steel bars beyond the expected plastic hinge regions using steel-headed couplers. The bottom ends are embedded and fixed in the foundation. The SMA bars are designed to be unbonded by steel or plastic ducts from the surrounding concrete to allow free and uniform axial deformation. The SMA bars do not transfer tensile stress into

Table 1 Measured mechanical properties for NiTi superelastic SMA bar	Parameters	Measured values	
		Tension	Compression
	Austenite modulus of elasticity, k_1 (GPa)	30.7	41.4
	Post yield stiffness, k_2 (GPa)	1.7	7.8
	Austenite yield strength, f_y (MPa)	460.7	621.3
	Lower plateau stress factor, β	0.50	0.74
	Recoverable superelastic strain, ε_r (%)	6.0	5.0
The definitions of parameters are introduced in Fig. 7a	Secondary post-yield stiffness ratio, α	0.50	0.64
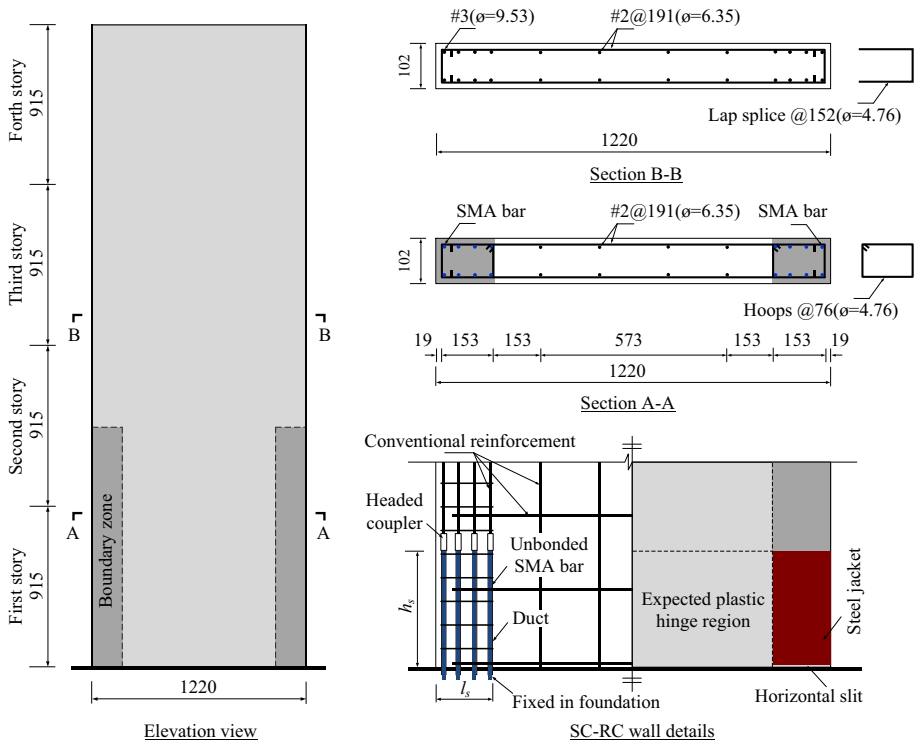
Fig. 5 SC–RC wall dimensions and reinforcement details (unit: mm)

the concrete, thereby reducing cracking in the wall boundary zones. Moreover, the duct can prevent the potential buckling of SMA bars under compression. Horizontal slits (gaps) are designed symmetrically at the wall-foundation interface where the SMA bars are placed. The rest of the central wall-foundation region is cast together with the foundation. The cast wall-foundation joint can also provide dowel forces to prevent the shear sliding of the wall panel. If the horizontal slit is designed throughout the wall panel base (regarded as a rocking wall), then additional measures should be considered to prevent shear sliding. For example, steel shear dowels were successfully reported in past studies (Restrepo and Rahman 2007; Lu et al. 2017). The horizontal slit separating the wall and foundation can minimize the tensile cracks in the boundary zones, in which the tension force is mainly undertaken by the SMA bars. This design can help achieve SC behavior. Steel jackets are armored in the wall boundary zones to avoid damage (e.g., spalling and crushing) at wall toes under cyclic loading (Mander and Cheng 1997; Guo et al. 2014). The SC restoring force in the SC–RC wall system is provided by the superelastic SMA bars and vertical loads, whereas the energy dissipation is contributed by the superelastic SMA bars and the cast wall-foundation region. If the horizontal-through slit is designed at the wall panel base (a rocking wall), then the superelastic SMA bars alone offer total energy dissipation.

Figure 5 shows that the unbonded superelastic SMA bars are placed only at the lower regions of two boundary zones to minimize cost. The height of SMA bars h_s can be evaluated using the plastic hinge length l_p of the shear wall as follows (Paulay and Priestley 1993):

$$l_p = 0.2l_w + 0.044h_w, \tag{1}$$

where l_w is the wall length, and h_w is the wall height. The height of SMA bars $h_s = 1.5l_p$ is recommended to avoid damage to the connections between the SMA bars and the steel rebars. The horizontal length of the boundary zones l_s can be determined according to ACI 318 provisions (2014) for the boundary elements of RC walls.

The RW2 is selected as a reference model to compare with the performance of the proposed SC–RC wall. The SC–RC wall is designed to have flexural capacity similar to that of the RW2 specimen. As aforementioned, the SC–RC wall has geometric and material properties, reinforcement details, and axial load similar to those of the RW2 specimen, except for the 8 Ø9.2 mm unbonded SMA bars used in the lower boundary zones. The height of SMA bars h_s is 600 mm and the horizontal length l_s is 172 mm. Slit length is initially considered as 172 mm, which is equal to the horizontal length of the boundary zone; however, the slit length is changed in the parametric studies of Sect. 6.

4 Development of the numerical model

4.1 Modeling of SC–RC wall

The modeling and nonlinear analyses in this study are conducted using the finite-element program *OpenSees* (Mazzoni et al. 2016). Figure 6 shows the numerical model that considers the interaction among axial force, bending moment, and shear force. The four-node
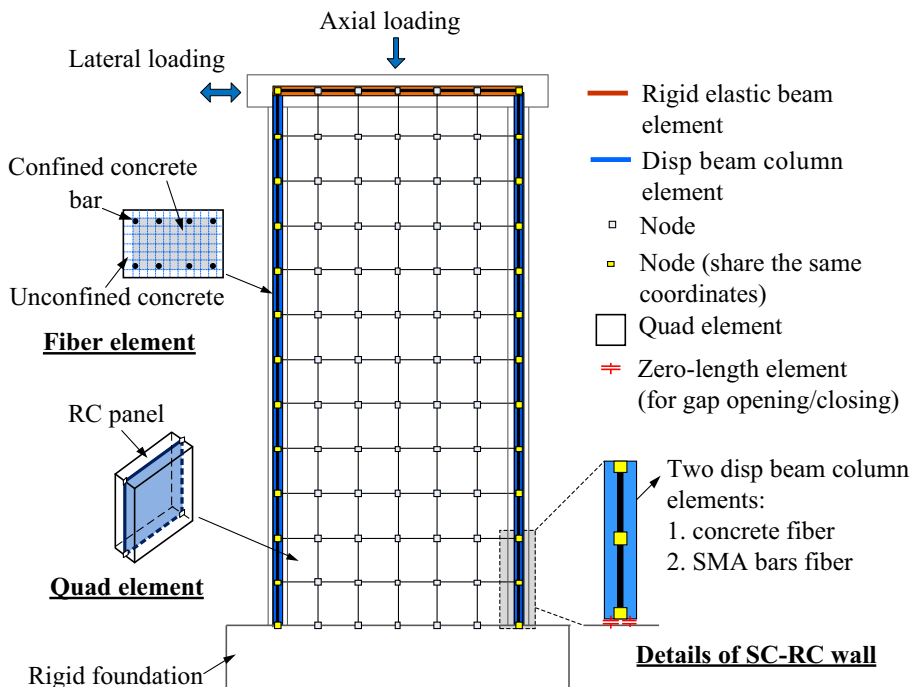
Fig. 6 Modeling of SC–RC wall

plane-stress rectangular quad element with eight degrees of freedom (DOFs) is used to model the wall panel. The boundary zones of the conventional RC wall (i.e., RW2) are modeled using the displacement-based beam–column fiber element, which can ensure reasonable levels of accuracy and convergence efficiency (Mo et al. 2008). In the SC–RC wall, the same modeling approach is adopted for the conventional reinforcement zones above the boundary zones, whereas two separate fiber sections (namely, concrete and SMA bar fibers) are employed to model the boundary zones with the unbonded SMA bars because the plane section assumption is no longer satisfied in the unbonded boundary zones during the cyclic response. SMA bars are modeled using the displacement-based beam–column fiber element with three integration points along each element. The lower ends are fixed to the foundation. Although the unbonded SMA elements are mainly subjected to axial force under cyclic loading, providing a small number of integration points could avoid numerical issues (Guerrini et al. 2015). The gap opening at the wall-foundation interface is modeled using multiple non-linear zero-length elements (compression only). The command equalDOF in *OpenSees* is used to model the deformation compatibility between the boundary zones and the wall panel. Elastic beam–column elements are used to model the rigid loading beam, wherein compressive and lateral loads are applied. The wall panel is cast together with the foundation except for the boundary zones. Thus, all nodes at the wall base are entirely fixed.

4.2 Material constitutive relationships

The concrete in the numerical model is divided into the unconfined (concrete cover) and confined concrete zones to describe the confining effect of the hoops in the boundary elements. The uniaxial Concrete02 material model in *OpenSees* is used as the constitutive model for the unconfined and confined concretes. The compression stress–strain curve of the confined concrete is defined by the Chang and Mander model (1994), wherein the peak and crushing points are determined at 51.8 MPa at the 0.0045 strain and 35.4 MPa at the ultimate strain of 0.016.

The RC wall panel is modeled with the plane stress RC material model, named FAReinforcedConcretePlaneStress in *OpenSees*, which is based on the cyclic softened membrane model (CSMM) proposed by Mansour and Hsu (2005a, b). The cracked reinforced concrete is assumed a continuum material in a smeared crack model. The Steel02 material model with a strain-hardening ratio of 1% is used for longitudinal reinforcement in the boundary zones. Parameters R_0, cR_1, and cR_2, which control transition from elastic to plastic branches, are set as 18.5, 0.925, and 0.15, respectively.

Figure 7a shows that self-centering material is used to model the unbonded SMA bars in the SC–RC wall to describe the main flag-shaped characteristic and superelastic stress–strain response (Tazarv and Saiidi 2015; Qiu and Zhu 2017). The yield-like stress f_y is the initiation of forward (austenite to martensite) phase transformation; after the forward phase transformation stress f_y, the slope changes from the austenite modulus k_1 to post-yield stiffness k_2 and continues up to the superelastic strain limit (i.e., the maximum recoverable strain) ε_r. The loading path beyond ε_r follows a slope of second strain-hardening k_3 up to ultimate strain ε_u. Upon unloading from any strain less than ε_r, the slope of the unloading path is k_1 until the stress reduction reaches βf_y.

Several factors (such as temperature, strain rate, and fatigue life), which may affect the superelastic behavior of SMA bars, cannot be explicitly considered in this simple model. The temperature variation will affect the macroscopic transformation properties of SMA devices if they are installed outdoors (Torra et al. 2014). In this study, however, the SMA
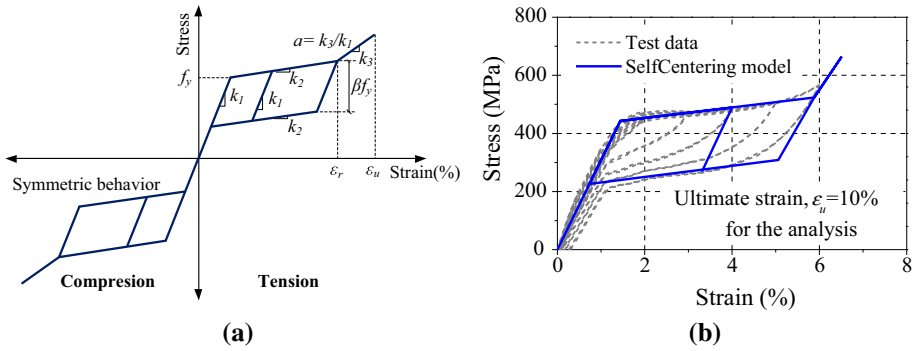
Fig. 7 Numerical model of superelastic SMA bar: **a** uniaxial stress–strain relationship; **b** comparison between the test data and self-centering model in tension

bars embedded in the RC wall are assumed located in an indoor environment. Thus, the SMA bars are not subjected to severe temperature variations due to the insulation effect of concrete (Tazarv and Saiidi 2015). Moreover, the tests conducted by the authors indicate that the strength, equivalent damping ratio, and SC property of SMA bars are insensitive to loading rates within the range of interest for seismic application (i.e., frequencies from 0.1 to 2 Hz). In addition, the fatigue life of SMA highly depends on chemical composition, manufacturing process, and loading conditions, etc. NiTi SMAs commonly exhibits high fatigue performance. In the current SC–RC wall system, the SMA bars are mainly subjected to tensile force in the boundary zones, whereas concrete undertakes compressive load under cyclic loading. Thus, Table 1 shows the parameters of self-centering material for SMA bar that are calibrated according to tensile behavior. Figure 7b shows the comparison between the test data and SC model.

The contact zero-length gap elements at the bottom of the boundary zones are modeled using elastic-no tension (ENT) material. This material allows compression-only behavior for concrete in the lower boundary zones of the SC–RC wall. Given the presence of armoured steel angle jackets in the gap of the wall-foundation, the zero-length element was defined with high stiffness compared with the adjoining elements (e.g., 100 times of modulus of elasticity of concrete).

4.3 RC wall simulation and model validation

The effectiveness of the numerical model is validated by comparing with the experiment of the RC wall (i.e., RW2) described in Thomsen and Wallace (2004). Figure 8 shows the cyclic loading protocol. The first drift level to be applied was approximately 0.1% and then increased up to 1.0% with an incremental step of 0.25%. The next drift level was 1.5% followed by another drift level of 1.0%. The drift was then increased up to 2.5% with an incremental step of 0.5%. The drift ratio is defined as the ratio of the lateral displacement at the roof level to the height of the wall (i.e. 3660 mm). The simulation results of the RW2 specimen are discussed in this subsection.

RW2 was tested with an average axial load of 0.07 $A_g f_c$ (378 kN). The reversed loading protocols used displacement control and typically consisted of two cycles at each level. The first cycle at a lateral drift ratio of 0.5% resulted in flexural cracks in the bottom two

**Fig. 8** Cyclic loading protocol for RC wall
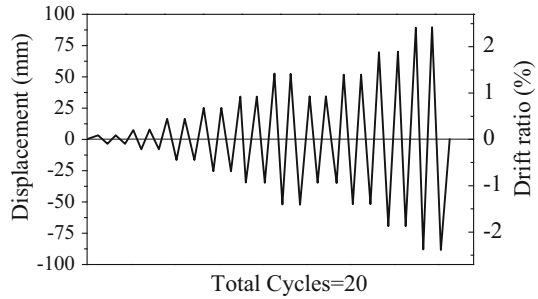
stories. Vertical splitting at the bottom of the wall was initiated in the cycle of 1.0% drift ratio. Major concrete spalling at both boundaries was recorded at 2.5% drift. Spalling occurred over the bottom 254 and 178 mm along the wall sides. The observed damage in RW2 was dominated by a flexural-failure mode.

Figure 9 compares the experimental results reported in Thomsen and Wallace (2004, 1995) and the numerical results simulated in this study, including the lateral force-top displacement responses and the lateral force-shear distortion response in the first story, wherein the shear distortion is calculated using the diagonal deformation data (i.e. X configuration) recorded in the first story level. Figure 10 displays the strain profiles calculated over 229 mm gauge length at the base of the wall specimen. Good agreements can be observed between both results. The numerical model satisfactorily captures the measured global cyclic behavior and local response, including strength, stiffness degradation, hysteretic shape, residual displacement, and local strain profile. A slight difference in the initial stiffness between the experimental and numerical results is observed in tensile and compressive directions, which may be caused by assuming a rigid foundation in the numerical model.
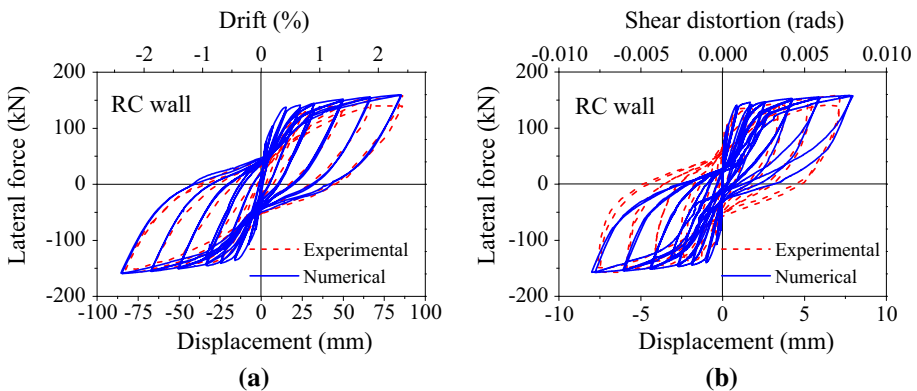
**Fig. 9** Comparison between experimental and numerical results for RW2

Fig. 10 Variation of strain profiles along the web in the horizontal direction
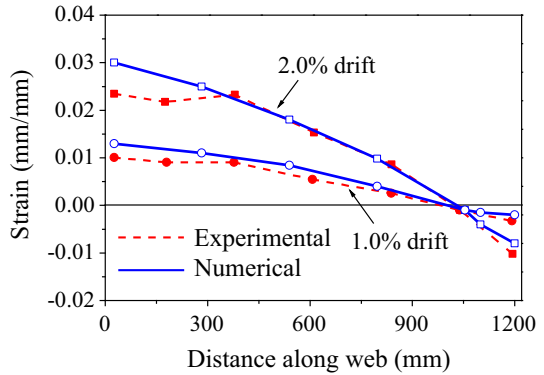
5 SC–RC wall simulation

The general geometric and design parameters of the SC–RC wall remained consistent with the RC wall, except for replacing steel rebars with the unbonded SMA bars in the boundary zones and having slits under the boundary zones. To compare the hysteretic behavior of the SC–RC wall to the conventional RC wall (RW2), the same cyclic loading protocol is used in the numerical study. Figure 11a compares the hysteretic curves of the RC and SC–RC walls. The SC–RC wall exhibits a flag-shaped behavior because of the use of unbonded superelastic SMA bars in the boundary zones compared with the typical fat hysteretic curves of conventional RC wall. The energy dissipation in the RC wall relies on the formation of a plastic hinge at the bottom of the wall with significant residual deformation. By contrast, the SC–RC wall exhibits a relatively less energy dissipation; however, residual deformation and strength degradation do not occur after 12 cycles up to 2.5% drift ratio.

For comparison, the concept of equal flexural capacity is adopted in the SC–RC wall design. Consequently, Fig. 11b shows that similar flexural strengths are obtained from the backbone curves of the two walls. The RC and SC–RC walls have similar initial stiffness in the low drift cycles. However, after the gap opening at the bottom of the SC–RC wall, the
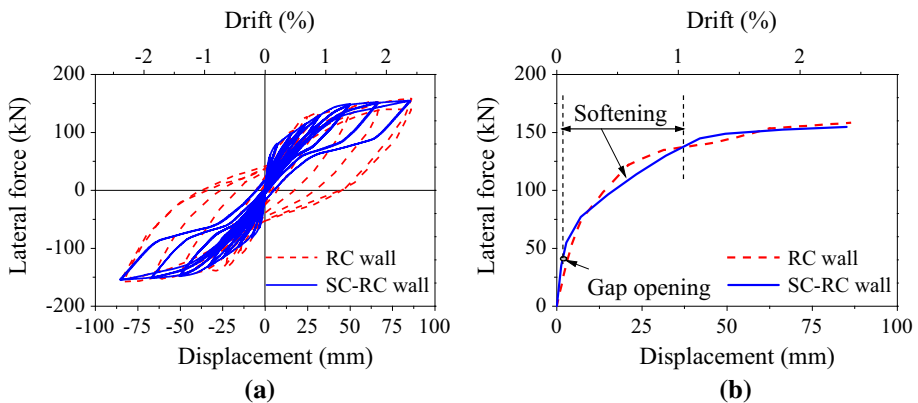
Fig. 11 Lateral force–displacement relationships of RC and SC–RC walls: **a** hysteretic curves; **b** backbone curves

tension in the boundary zone is only provided by the unbonded SMA bars, which have a relatively low austenite modulus of elasticity. This results in a slightly low stiffness of the SC–RC wall. The gradual reduction in the lateral stiffness shows a softening state in the backbone curves. The strength of the RC and SC–RC walls is comparable after yielding SMA or steel bars.

Figure 12 shows the strain curves of the outermost and innermost SMA bars in the boundary zones of the SC–RC wall. The SMA bars are mainly subjected to tension, and the maximum compressive strain of the outermost bars is only 0.2%. Most compressions in the boundary zones are undertaken by the concrete. As expected, all the SMA bars in the boundary zones yield under tension with the increasing loading amplitude. Compared with the outermost bars, the innermost SMA bars experience approximately 30% less strain. The peak strain of the outermost bars is approximately 3.3%. This peak strain, which is less than the superelastic strain limit of 6% commonly used in engineering, corresponds to the drift ratio of 2.5%. Therefore, the SC–RC wall has a sufficient capacity to be further loaded to a large displacement in the subsequent cycles. Compared with the RC wall (RW2) that was severely damaged after the 2.5% drift cycle, the SC–RC wall taking advantage of superelastic SMA bars demonstrates improved ductility.

6 Parametric studies of SC–RC wall

6.1 Selected parameters

Following the successful modeling and simulation of the aforementioned SC–RC wall, the influence of three design parameters, namely, axial compressive load ratio, slit length, and lower plateau stress factor of SMA, on the hysteretic performance of the SC–RC wall is investigated through parametric studies. The SC–RC wall parameters described in Sect. 3 are considered as the baseline case. Table 2 shows the changes in the three design parameters, which are determined according to the engineering practice or design code recommendations. For example, axial load ratios in practical RC walls have a range of $0 \leq P/A_g f_c \leq 0.15$ for low-to-moderate height buildings (Priestley et al. 2007). The bottom-slit length is also adjusted. When the slit length is 610 mm, the SC–RC wall becomes a rocking wall with its concrete base completely separated from the foundation by a through-gap formed. Parameter β, which is the ratio of the width of the hysteretic loop to
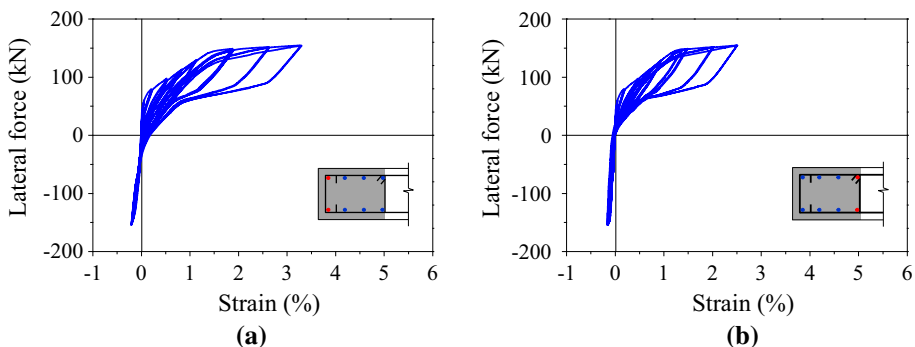
Fig. 12 Strain results of SMA bar in the boundary zones: **a** outermost bars; **b** innermost bars

Table 2 Range of parameters selected in the parametric study

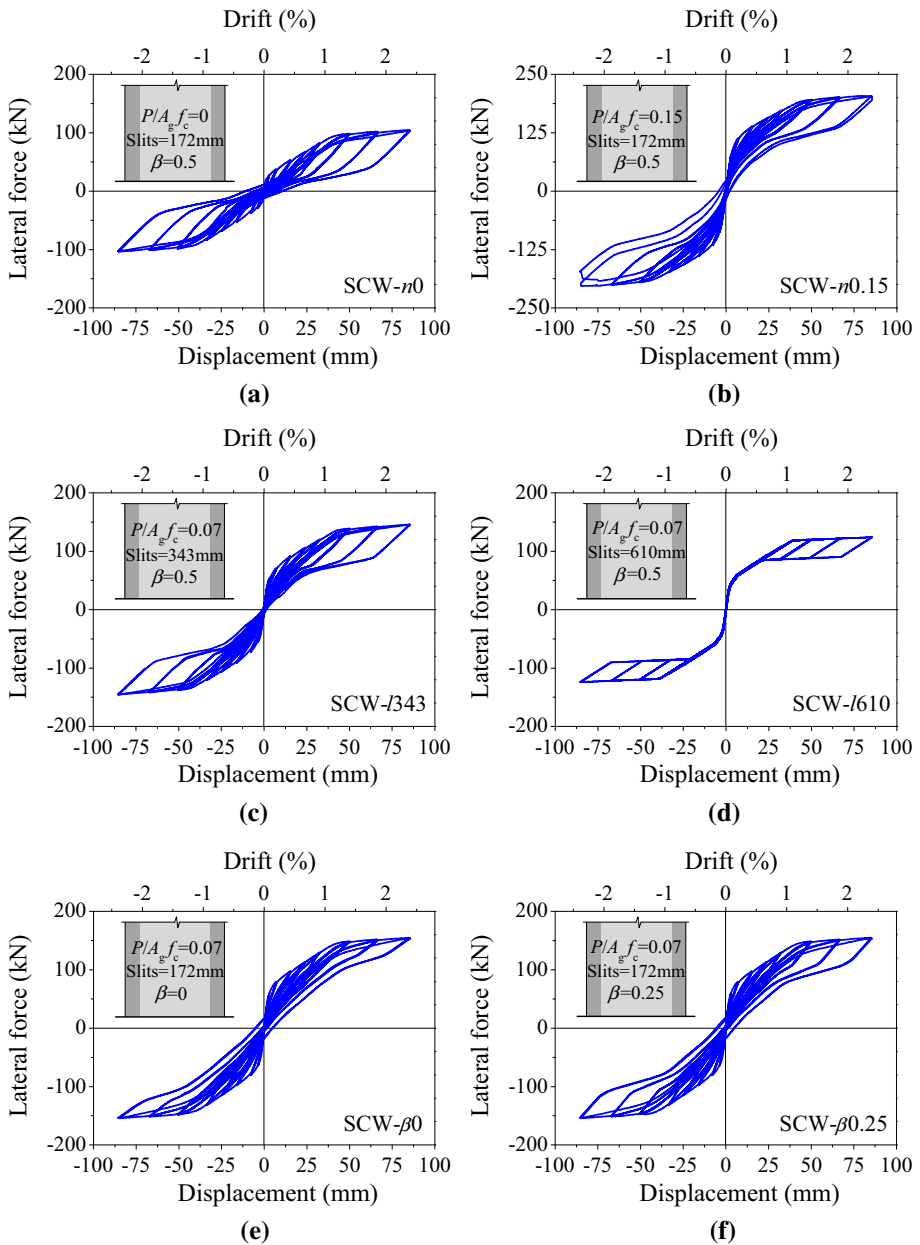| Specimen no.	Parameters		
	Axial load ratio ($n = P/A_g f_c$)	Slit length (mm)	Lower plateau stress factor, β
SCW-n0	0	172	0.5
SCW-n0.07[a]	0.07	172	0.5
SCW-n0.15	0.15	172	0.5
SCW-l172[a]	0.07	172	0.5
SCW-l343	0.07	343	0.5
SCW-l610	0.07	610	0.5
SCW-β0	0.07	172	0
SCW-β0.25	0.07	172	0.25
SCW-β0.5[a]	0.07	172	0.5

[a] These cases refer to the same baseline SC–RC wall

the loading plateau stress in the forward transformation (as shown in Fig. 7a), signifies the energy dissipation capacity of SMA bars under cyclic loading. The β range of 0–0.5 is selected to represent different energy dissipation levels. The value of $\beta = 0$ means that SMA bars do not dissipate energy and only provide the SC ability. The parameters of the baseline case are $n = 0.07$, $l = 172$ mm, and $\beta = 0.5$. Thus, the cases of SCW-n0.07, SCW-l172, and SCW-β0.5 refer to the same baseline SC–RC wall with the corresponding hysteretic behavior shown in Fig. 11. The cyclic loading protocol shown in Fig. 8 is applied to different SC–RC walls.

6.2 Lateral force–displacement response

Figure 13 shows the lateral force–displacement responses of numerical simulations with different parameters. The specimens show apparent flag-shaped hysteretic behavior. Figure 14 shows the comparison among the backbone curves of the specimens with different parameters. Figure 13a, b show that all design parameters are identical, except the axial load ratio n. The wall-foundation interfaces (in the boundary zones) remained closed until the lateral forces reach the imminent gap opening loads (referred to as F_{IGO}). The initial stiffness of SCW-n0, SCW-n0.07, and SCW-n0.15 are 27.1, 29.4, and 29.6 kN/mm, respectively. The corresponding displacements at the imminent gap opening state (D_{IGO}) of the three specimens are 0.2, 1.0, and 1.9 mm, respectively. Therefore, Fig. 14a shows that a high axial load ratio results in a high F_{IGO} and large D_{IGO}, but has a slight effect on the initial stiffness. The original SC–RC wall is designed with an axial load ratio of 0.07 (SCW-n0.07). Even a high axial load ratio of 0.15 can still ensure SC ability. The steel jacket in the wall boundary zones protects the corner concrete from crushing and increases the ultimate strain of concrete. Only minor strength degradation is observed in the cyclic loading behavior. Increasing the axial load ratio can also delay the yielding of SMA bars in tension and therefore improve the lateral strength of the SC wall.

Figure 13c, d show the effect of the bottom-slit length on the hysteretic behavior, whereas other parameters remained constant. SCW-l343 has an intermediate slit length, whereas the SCW-l610 has a through-gap at the wall-foundation interface, and thus is

Fig. 13 Lateral force–displacement responses of specimens with different parameters: **a** SCW-*n*0; **b** SCW-*n*0.15; **c** SCW-*l*343; **d** SCW-*l*610; **e** SCW-*β*0; **f** SCW-*β*0.25

regarded as a rocking wall system. Consequently, the energy dissipation in specimen SCW-*l*610 is solely contributed by the SMA bars located in the boundary zones. Figure 14b shows that the initial stiffness of these specimens is 29.4, 26.6, and 25.1 kN/mm. The bottom-slit length has slight effect on F_{IGO} and D_{IGO}. However, increasing the bottom-slit
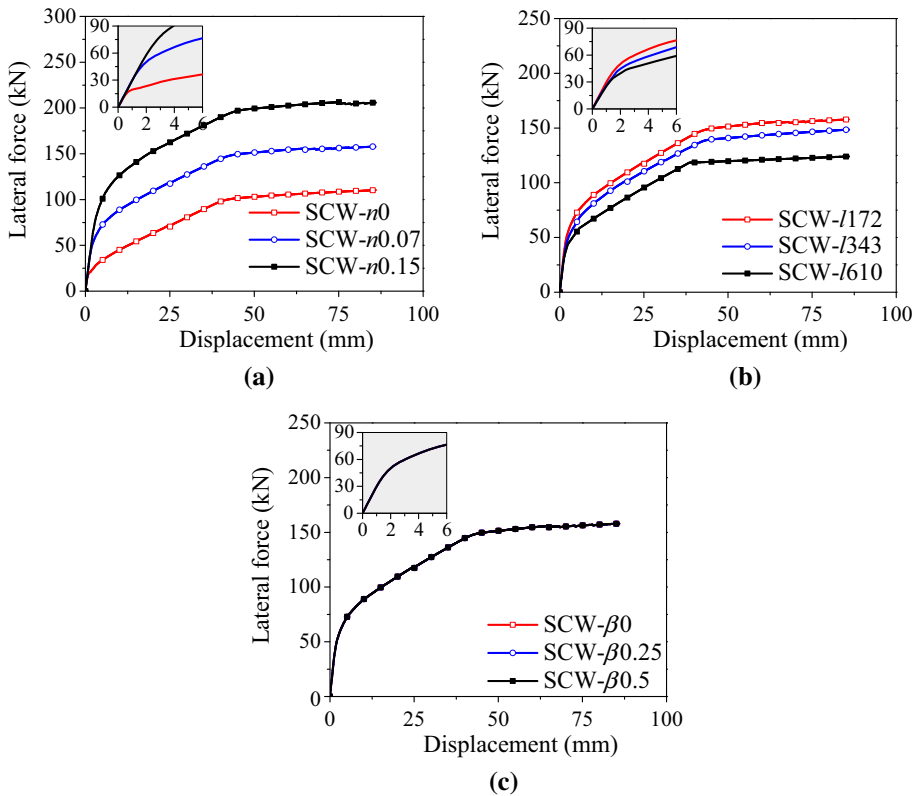
Fig. 14 Comparison among the backbone curves of the specimens with different parameters: **a** axial load ratio; **b** length of bottom slit; **c** lower plateau stress factor of SMA

length reduces the central cast wall-foundation region, and thereby decreases the ultimate strength of SC walls.

Figure 13e, f show that comparisons are performed among SCW-β0 and SCW-β0.25 to investigate the influence of the lower plateau stress factor of SMA (β) on hysteretic behavior. Energy is completely dissipated by the central wall region in SCW-β0 and the SMA bars only provide SC ability. SCW-β0.25 shows slightly fatter hysteretic loops after the SMA bar yielding (at approximately 1% drift) than SCW-β0 because of energy dissipation by the SMA bars. Figure 14c shows that the low plateau stress factor (β) has no effect on F_{IGO} and D_{IGO} but only affects energy dissipation capacity.

6.3 SC ability

The SC–RC walls exhibit typically flag-shaped behavior and have excellent SC ability compared with those of the RC wall. The residual drift ratio is an important index to indicate SC abilities. In this study, residual drift is defined as the drift ratio when the lateral force is completely unloaded at each loading level. The average residual drift ratio for two loading directions in each cycle is considered. Figure 15 shows the residual drift of each specimen, which correspond to different peak drifts. Before the cycle of 2.5% peak drift, all SC–RC walls, except the specimen SCW-n0, exhibit negligible residual deformation
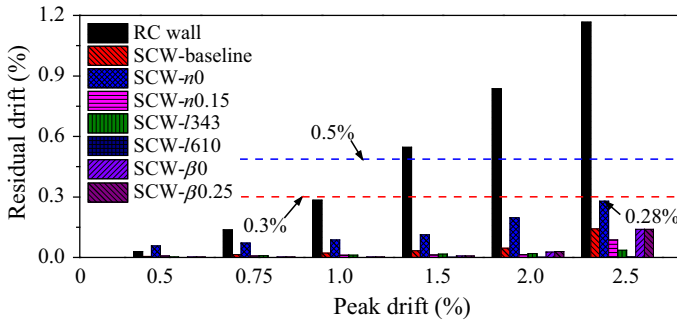
Fig. 15 Residual drift of each specimen under different peak drifts

that is less than 0.05%. The larger residual drift of SCW-$n0$ decreases the SC ability because of the low axial load, wherein the deformation recovery is provided by the SMA bars alone. However, a high axial load may not be beneficial because the increased axial load may cause increased inelastic damage to the RC wall (Henry et al. 2016a).

Residual deformation is caused by the inelastic damage in the bottom cast zone of the RC wall. Increasing the slit length at the wall base can reduce damage in the RC wall and thus benefit its SC ability. Compared with the residual drift of 0.14% of SCW-$l172$ after unloading from 2.5% peak drift, the corresponding residual drifts of SCW-$l343$ and SCW-$l610$ are 0.035 and 0.002%, respectively. Furthermore, the SMA stress factor β has almost no effect on the SC ability and only affects energy dissipation capacity (see more detailed discussion in Sect. 6.4).

Residual deformations or drift ratios have yet been formally introduced in most seismic design codes, but they have been gradually recognized as an important seismic performance index. At present, only the Japanese design specification sets up a residual drift limit of 1% for highway bridges (JRA 2002). The FEMA P-58-1 guideline (2012) presents four damage states (DS1–DS4) that range from the onset of non-structural damage to near collapse, which are related to residual drift ratios. The guideline presents the residual story drift limit of 0.5% (DS2) that allows repairs to non-structural and mechanical components and prevents the degradation in structural stability (collapse safety). Residual drift limit beyond 1% (DS3) is a threshold that may be uneconomical or infeasible to repair damaged structures. However, increasing number of studies suggested that a residual drift of beyond 0.5% should be considered as a limit, which may be more economical and practical to replace than repair a damaged building (McCormick et al. 2008; Erochko et al. 2011). Henry et al. (2016b) proposed multiple residual drift limits that correspond to different hazard levels for SC concrete walls. The allowable residual drifts are equal to 0.2% for design-level earthquakes and up to 0.3% when subjected to the maximum considered earthquakes. Figure 15 shows two limit values, namely, 0.3 and 0.5%, which are used as performance evaluation indicators. The maximum residual drift value of SCW-$n0$ is 0.28%, whereas the rest of the SC–RC walls have less residual drifts than the suggested limit values.

6.4 Energy dissipation

The equivalent viscous damping ratio (ξ_{eq}) is calculated in the second cycle at each displacement level to quantify the energy dissipation of each specimen,

$$\xi_{eq} = \frac{E_D}{4\pi E_S} = \frac{E_D}{2\pi K_s d_m^2}, \tag{2}$$

where E_D is the total energy dissipated per cycle, E_S is the elastic strain energy at the peak displacement, K_s is the secant stiffness at the maximum displacement, and d_m is the maximum loading displacement of the cycle. In an entire hysteretic loop, K_s and d_m are taken as the average values of the positive and negative loading paths.

Figure 16 compares the variation of equivalent viscous damping ratio of each specimen with increasing loading amplitudes. The equivalent viscous damping ratio of the conventional RC wall ($\xi_{eq} = 21.3\%$ at 2.5% drift) is higher than those of the SC–RC wall systems with SMA bars. The SMA bars in the boundary zones do not yield at the early loading stage (below 1% peak drift), and thus the equivalent viscous damping ratio is mainly contributed by the central cast wall-foundation region. Beyond the 1% peak drift, however, the SMA bars exhibit flag-shaped hysteretic responses, and the equivalent viscous damping ratio increases accordingly. In addition, SCW-n0 without axial load can increase the equivalent viscous damping ratio ($\xi_{eq} = 12.2\%$ at 2.5% drift) at the cost of decreased SC ability. ACI ITG-5.1 (2008) uses the relative energy dissipation ratio, β_h, which is defined as the energy dissipation of the SC system to that of a bilinear elastoplastic system with the same drift. This process quantifies the energy dissipation of the unbonded post-tensioned precast shear wall. ACI ITG-5.1 requires that the relative energy dissipation ratio shall not be less than 0.125 at a given target drift, which can be converted into the equivalent viscous damping ratio by $\xi_{eq} = 2\beta_h/\pi$. Figure 16 shows that the equivalent viscous damping ratio of the SCW-baseline wall at 2.5% drift ratio is 8.1%, which satisfies the required value. However, SCW-l610 (rocking wall) relies on the SMA bars alone for energy dissipation, and thus shows the smallest equivalent viscous damping ratio ($\xi_{eq} = 4.4\%$ at 2.5% drift). This finding means that additional energy dissipating mechanisms shall be added to the rocking wall in practice.

Fig. 16 Equivalent viscous damping ratio of each specimen
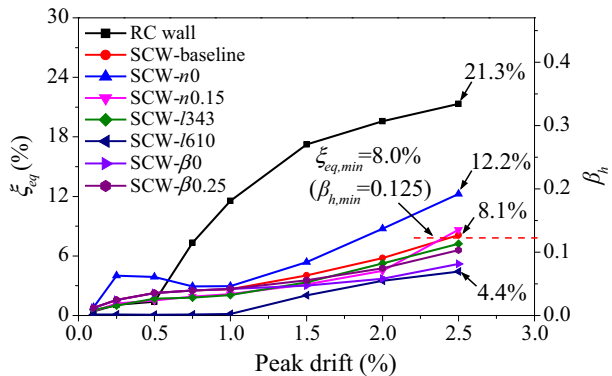
6.5 Damage regions

The damage of traditional RC walls typically concentrates in the bottom corner regions. The horizontal slits in the proposed SC–RC wall system are designed at the wall-foundation interface below the boundary zones. Tension transmission to the concrete in the lower boundary zones can be avoided by allowing the opening/closing behavior of the gap. Moreover, steel jackets armoured in the wall boundary zones can prevent any compressive damage at wall toes from spalling and crushing during the cyclic loading. The tensile forces of the unbonded SMA bars are directly transmitted to the concrete in the upper boundary zones and result in minor damage. Therefore, the potential damage regions are moved to the upper boundary and the corner regions of the central zone (as shown in Fig. 17). The damages of SCW-*l*172 (SCW-baseline) and SCW-*l*610 (rocking wall) will be evaluated through the average strain measured by hypothetic displacement transducers with a length of 200 mm (as shown in Fig. 17).

Figure 18 shows the average strains of the corner regions of the central zone of the wall ($S_{central}$) and the upper boundary region ($S_{boundary}$) in the two specimens. Kowalsky (2000) recommended the strain limits for "serviceability" (no need for repair after earthquake) and "damage control" limit states (damage is repairable). The steel tensile strain limits of "serviceability" and "damage control" are 0.015 and 0.06, respectively. The concrete compressive strain limits of "serviceability" and "damage control" are 0.004 and 0.018, respectively. Furthermore, the commonly used superelastic strain limit of SMA is 6%.

The maximum tensile strains of $S_{central}$ and $S_{boundary}$ that correspond to the 2.5% drift in SCW-*l*172 are 0.35 and 0.008, respectively, whereas the maximum compressive strains of $S_{central}$ and $S_{boundary}$ are -0.0021 and -0.00045, respectively. Only repairable damage occurs in the central wall and repair is not needed in the upper boundary concrete for SCW-*l*172. As shown by the comparison between Figs. 8 and 18a, the corresponding drift ratio is 1% when the tensile strains of $S_{central}$ reach the serviceability state limit. In other words, SCW-*l*172 does not need repair when loaded within the 1% drift loading level.

Deformation in SCW-*l*610 is mainly caused by the gap opening/closing in the rocking behavior, and no concrete damage occurred in the central zone. The maximum tensile and compressive strains of $S_{boundary}$ are 0.015 and -0.00045 with 2.5% drift. Only minor cracks occur in the upper boundary concrete and no repair is needed in SCW-*l*610. The serviceability limit state is satisfied up to the 2.5% drift.
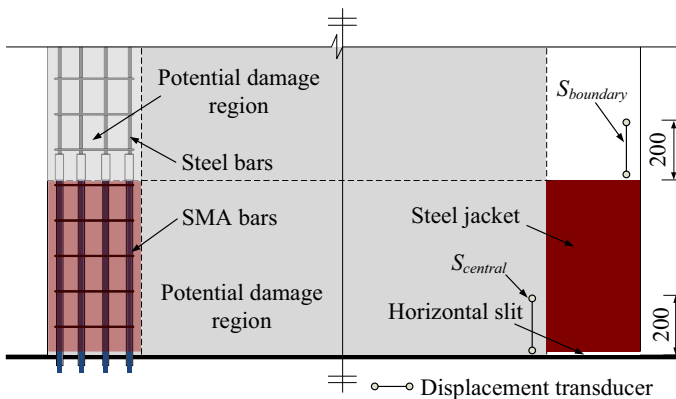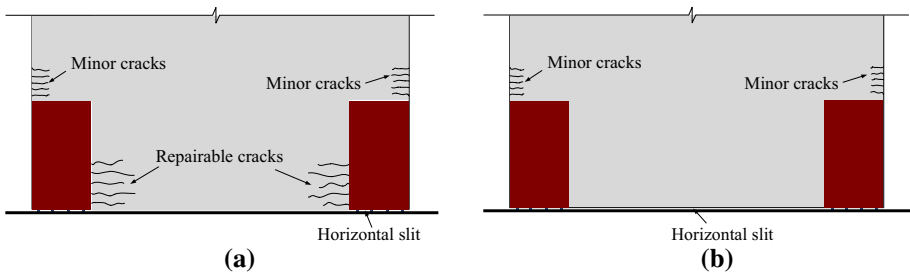

Fig. 17 Potential damage regions in SC–RC wall
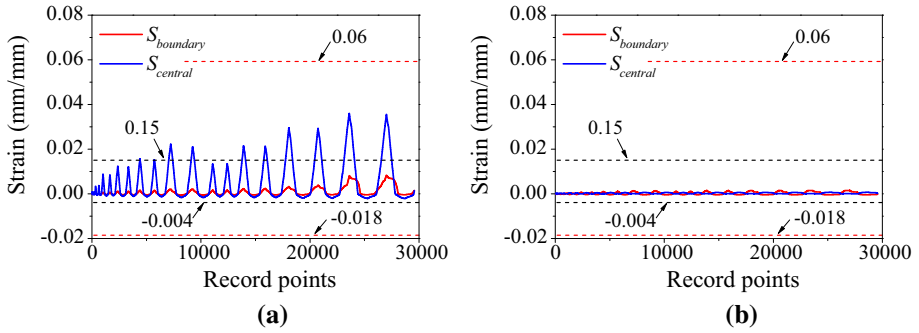
Fig. 18 Average strains of damage regions: **a** SCW-*l*172; **b** SCW-*l*610
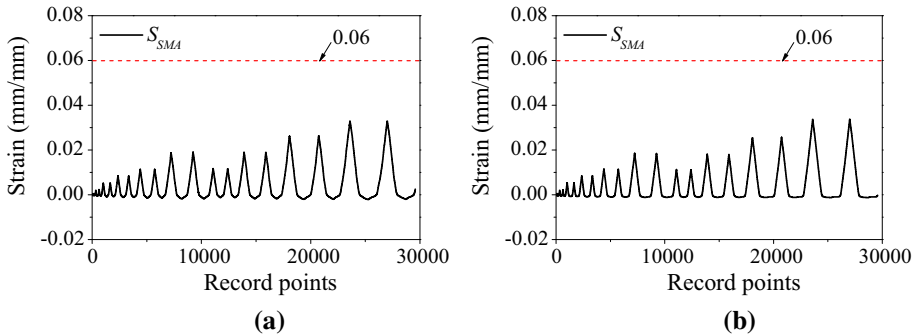
Fig. 19 Strains of outermost SMA bars in boundary zones: **a** SCW-*l*172; **b** SCW-*l*610

Fig. 20 Concrete damage patterns: **a** SCW-*l*172; **b** SCW-*l*610

Figure 19 shows the outermost SMA strains in the boundary zones of two specimens. The peak tension strains of two specimens are approximately 3.3%, which correspond to the drift ratio of 2.5%. This value is less than 6% of the strain limit of the superelastic SMA bars commonly used in practice.

Figure 20 shows the schematic of the likely concrete damage patterns in two specimens. SCW-*l*172 can achieve seismic resilience after severe earthquakes because of the negligible residual drift (as discussed in Sect. 6.3) and only repairable damage in the central wall. SCW-*l*610 is associated with only minor concrete damage that requires no repair after

severe earthquakes. However, additional energy dissipation mechanisms may be required in SCW-*l*610 when used in practice (as discussed in Sect. 6.4).

7 Conclusions

This study investigates the seismic behavior of novel SC–RC walls using superelastic SMA bars with large strain recovery and excellent fatigue property. The SC–RC walls utilize the buckling-restrained superelastic NiTi bars in the boundary zones to reduce the residual deformation after cyclic loading. The mechanical properties of SMA bars and the SC–RC wall design are described. A numerical SC–RC wall model is established and validated by comparing with testing results. Parametric studies are then performed to investigate the effects of axial compressive load ratio, the bottom slit length, and the lower plateau stress factor of SMA on the hysteretic behavior of the SC–RC walls.

The SC–RC walls exhibit flag-shaped responses caused by the use of unbonded superelastic SMA bars in the boundary zones compared with the typical hysteretic curves of conventional RC walls. Energy dissipation in conventional RC walls relies on the plastic deformation at the bottom of walls and results in significant residual deformation. Although the SC–RC walls dissipate relatively less energy through hysteretic loops, they exhibit almost no residual deformation after loading cycles with the peak drift of 2.5%. In terms of the 2.5% drift, the SMA peak strain bar is only 3.3%, which is lesser than the commonly adopted maximum SMA recoverable strain (i.e., 6%). This finding implies a capacity margin in ductility that will enable the SC–RC walls to be loaded to a greater displacement.

The potential damage in two representative specimens, namely, SCW-*l*172 and SCW-*l*610, with different bottom slit lengths is evaluated, wherein the latter represents a rocking wall system with a through gap at the wall-foundation interface. SCW-*l*172 at the peak drift level of 2.5% exhibits negligible residual drift and repairable damage in the central concrete wall. SCW-*l*610 exhibits negligible residual drift and minor damage without any need for repair. Both have potential to achieve resilient seismic design under severe earthquakes. However, additional energy dissipating devices may be required in the practical use of SCW-*l*610.

The SC–RC walls in this study are designed based on a conventional RC wall, wherein the specimen dimensions, material properties, reinforcement details, and loading protocols are similar to the original RC wall. However, such a design does not represent an optimal design for the SC–RC walls. Future studies should explore ways on how to establish a resilient seismic design method.

References

ACI (American Concrete Institute) (2008) Acceptance criteria for special unbonded post-tensioned precast structural walls based on validation testing. ACI ITG-5.1-07, Farmington Hills, MI

ACI (American Concrete Institute) (2014) Building code requirements for structural concrete (ACI 318-14) and commentary on building code requirements for structural concrete (ACI 318R-14). ACI Committee 318, Farmington Hills, MI

Alam MS, Nehdi M, Youssef MA (2009) Seismic performance of concrete frame structures reinforced with superelastic shape memory alloys. Smart Struct Syst 5(5):565–585

Araki Y, Shrestha KC, Maekawa N, Koetaka Y, Omori T, Kainuma R (2016) Shaking table tests of steel frame with superelastic Cu-Al-Mn SMA tension braces. Earthq Eng Struct D 45(2):297–314

Bradley BA, Dhakal RP, Mander JB, Li L (2008) Experimental multi-level seismic performance assessment of 3D RC frame designed for damage avoidance. Earthq Eng Struct D 37(1):1–20

Bruneau M, Reinhorn A (2007) Exploring the concept of seismic resilience for acute care facilities. Earthq Spectra 23(1):41–62

Casciati S, Faravelli L (2008) Structural components in shape memory alloy for localized energy dissipation. Comput Struct 86(3):330–339

Casciati S, Faravelli L (2009) A passive control device with SMA components: from the prototype to the model. Struct Control Hlth 16(7–8):751–765

Casciati S, Faravelli L, Vece M (2017) Investigation on the fatigue performance of Ni-Ti thin wires. Struct Control Hlth 24(1):e1855

CEN (European Committee for Standardization) (2004) Design of structures for earthquake resistance- Part 1: General rules, seismic actions and rules for buildings. Eurocode 8, Brussel, Belgium

Chang GA, Mander JB (1994) Seismic energy based fatigue damage analysis of bridge columns: Part I-Evaluation of seismic capacity. Technical Report NCEER-94-0006, Multidisciplinary Center for Earthquake Engineering Research, University at Buffalo, New York

DesRoches R, McCormick J, Delemont M (2004) Cyclic properties of superelastic shape memory alloy wires and bars. J Struct Eng 130(1):38–46

Di Cesare A, Ponzo FC, Nigro D, Pampanin S, Smith T (2017) Shaking table testing of post-tensioned timber frame building with passive energy dissipation systems. Bull Earthq Eng. doi:10.1007/s10518-017-0115-9

Dolce M, Cardone D, Ponzo FC (2007) Shaking-table tests on reinforced concrete frames with different isolation systems. Earthq Eng Struct D 36(5):573–596

Erochko J, Christopoulos C, Tremblay R, Choi H (2011) Residual drift response of SMRFs and BRB frames in steel buildings designed according to ASCE 7-05. J Struct Eng 137(5):589–599

Fang C, Yam MCH, Lam ACC, Xie LK (2014) Cyclic performance of extended end-plate connections equipped with shape memory alloy bolts. J Constr Steel Res 94:122–136

FEMA (Federal Emergency Management Agency) (2012) Seismic performance assessment of buildings: volume 1-methodology, FEMA P-58-1, Washington, D.C

Graesser EJ, Cozzarelli FA (1991) Shape-memory alloys as new materials for aseismic isolation. J Eng Mech 117(11):2590–2608

Guerrini G, Restrepo JI, Vervelidis A, Massari M (2015) Self-centering precast concrete dual-steel-shell columns for accelerated bridge construction: seismic performance, analysis, and design. Technical Report 2015/13, Pacific Earthquake Engineering Research Center, University of California, Berkeley, California

Guo T, Zhang GD, Chen C (2014) Experimental study on self-centering concrete wall with distributed friction devices. J Earthq Eng 18(2):214–230

Hashemi A, Masoudnia R, Quenneville P (2016) Seismic performance of hybrid self-centring steel-timber rocking core walls with slip friction connections. J Constr Steel Res 126:201–213

Henry RS, Sritharan S, Ingham JM (2016a) Finite element analysis of the PreWEC self-centering concrete wall system. Eng Struct 115:28–41

Henry RS, Sritharan S, Ingham JM (2016b) Residual drift analyses of realistic self-centering concrete wall systems. Earthq Struct 10(2):409–428

Holden T, Restrepo J, Mander JB (2003) Seismic performance of precast reinforced and prestressed concrete walls. J Struct Eng 129(3):286–296

Iqbal A, Pampanin S, Palermo A, Buchanan AH (2015) Performance and design of LVL walls coupled with UFP dissipaters. J Earthq Eng 19(3):383–409

JRA (Japan Road Association) (2002) Design specifications of highway bridges, Tokyo

Kam WY, Pampanin S, Palermo A, Carr AJ (2010) Self-centering structural systems with combination of hysteretic and viscous energy dissipations. Earthq Eng Struct D 39(10):1083–1108

Kowalsky MJ (2000) Deformation limit states for circular reinforced concrete bridge columns. J Struct Eng 126(8):869–878

Kramer A, Barbosa AR, Sinha A (2016) Performance of steel energy dissipators connected to cross-laminated timber wall panels subjected to tension and cyclic loading. J Struct Eng 142(4):E4015013

Lu XL, Dang XL, Qian J, Zhou Y, Jiang HJ (2017) Experimental study of self-centering shear walls with horizontal bottom slits. J Struct Eng 143(3):04016183

Ma HW, Cho CD (2008) Feasibility study on a superelastic SMA damper with re-centring capability. Mat Sci Eng A 473(1–2):290–296

Mander JB, Cheng C-T (1997) Seismic resistance of bridge piers based on damage avoidance design. Technical Report NCEER-97-0014, U.S. National Center for Earthquake Engineering Research (NCEER), Dept. of Civil and Environmental Engineering, State Univ. of New York at Buffalo, Buffalo, NY

Mansour M, Hsu TTC (2005a) Behavior of reinforced concrete elements under cyclic shear. I: experiments. J Struct Eng 131(1):44–53

Mansour M, Hsu TTC (2005b) Behavior of reinforced concrete elements under cyclic shear. II: theoretical model. J Struct Eng 131(1):54–65

Marquis F, Kim JJ, Elwood KJ, Chang SE (2017) Understanding post-earthquake decisions on multi-storey concrete buildings in Christchurch. N Z B Earthq Eng 15(2):731–758

Mazzoni S, McKenna F, Scott MH, Fenves GL (2016) Open system for earthquake engineering simulation (OpenSees) command language manual (Available from: http://opensees.berkeley.edu/wiki/index.php/Command_Manual) Pacific Earthquake Engineering Research Center, Univ. of California, Berkeley, CA

McCormick J, Tyber J, DesRoches R, Gall K, Maier HJ (2007) Structural engineering with NiTi. II: mechanical behavior and scaling. J Eng Mech 133(9):1019–1029

McCormick J, Aburano H, Ikenaga M, Nakashima M (2008) Permissible residual deformation level for building structures considering both safety and human elements. In: Proceedings of the 14th World Conference on Earthquake Engineering, Beijing, China. Paper ID 05-06-0071

Mo YL, Zhong J, Hsu TTC (2008) Seismic simulation of RC wall-type structures. Eng Struct 30(11):3167–3175

NIST (National Institute of Standards and Technology) (2014) Recommendations for seismic design of reinforced concrete wall buildings based on studies of the 2010 Maule, Chile earthquake. NIST GCR 14-917-25, NEHRP Consultants Joint Venture, Gaithersburg, MD

Ozbulut OE, Silwal B (2016) Performance assessment of buildings isolated with S-FBI system under near-fault earthquakes. Smart Struct Syst 17(5):709–724

Paulay T, Priestley MJN (1993) Stability of ductile structural walls. ACI Struct J 90(4):385–392

Priestley MJN, Calvi GM, Kowalsky MJ (2007) Displacement-based seismic design of structures. IUSS Press, Pavia

Qian H, Li HN, Song GB (2016) Experimental investigations of building structure with a superelastic shape memory alloy friction damper subject to seismic loads. Smart Mater Struct 25(12):125025

Qiu CX, Zhu SY (2017) Shake table test and numerical study of self-centering steel frame with SMA braces. Earthq Eng Struct D 46(1):117–137

Restrepo J, Rahman A (2007) Seismic performance of self-centering structural walls incorporating energy dissipators. J Struct Eng 133(11):1560–1570

Saiidi MS, Wang HY (2006) Exploratory study of seismic response of concrete columns with shape memory alloys reinforcement. ACI Struct J 103(3):436–443

Saiidi MS, Sadrossadat-Zadeh M, Ayoub C, Itani A (2007) Pilot study of behavior of concrete beams reinforced with shape memory alloys. J Mater Civil Eng 19(6):454–461

Saiidi MS, O'Brien M, Sadrossadat-Zadeh M (2009) Cyclic response of concrete bridge columns using superelastic Nitinol and bendable concrete. ACI Struct J 106(1):69–77

Shook DA, Roschke PN, Ozbulut OE (2008) Superelastic semi-active damping of a base-isolated structure. Struct Control Hlth 15(5):746–768

Smith BJ, Kurama YC, McGinnis MJ (2011) Design and measured behavior of a hybrid precast concrete wall specimen for seismic regions. J Struct Eng 137(10):1052–1062

Speicher MS, DesRoches R, Leon RT (2011) Experimental results of a NiTi shape memory alloy (SMA)-based recentering beam-column connection. Eng Struct 33(9):2448–2457

Sritharan S, Aaleti S, Henry RS, Liu KY, Tsai KC (2015) Precast concrete wall with end columns (PreWEC) for earthquake resistant design. Earthq Eng Struct D 44(12):2075–2092

Tazarv M, Saiidi MS (2015) Reinforcing NiTi superelastic SMA for concrete structures. J Struct Eng 141(8):04014197

Thomsen JH, Wallace JW (1995) Displacement-based design of reinforced concrete structural walls: Experimental studies of walls with rectangular and T-shaped cross sections. Rep. No. CU/CEE-95/06, Department of Civil and Environmental Engineering, Clarkson University, Potsdam, N.Y

Thomsen JH, Wallace JW (2004) Displacement-based design of slender reinforced concrete structural walls-experimental verification. J Struct Eng 130(4):618–630

Toranzo LA, Restrepo JI, Mander JB, Carr AJ (2009) Shake-table tests of confined-masonry rocking walls with supplementary hysteretic damping. J Earthq Eng 13(6):882–898

Torra V, Carreras G, Casciati S, Terriault P (2014) On the NiTi wires in dampers for stayed cables. Smart Struct Syst 13(3):353–374

Tzimas AS, Kamaris GS, Karavasilis TL, Galasso C (2016) Collapse risk and residual drift performance of steel buildings using post-tensioned MRFs and viscous dampers in near-fault regions. B Earthq Eng 14(6):1643–1662

Vasdravellis G, Karavasilis TL, Uy B (2013) Finite element models and cyclic behavior of self-centering steel post-tensioned connections with web hourglass pins. Eng Struct 52:1–16

Wang W, Fang C, Liu J (2017) Self-centering beam-to-column connections with combined superelastic SMA bolts and steel angles. J Struct Eng 143(2):04016175

Wikipedia (2017) https://en.wikipedia.org/wiki/Hotel_Grand_Chancellor,_Christchurch

Wolski M, Ricles JM, Sause R (2009) Experimental study of a self-centering beam-column connection with bottom flange friction device. J Struct Eng 135(5):479–488

Youssef MA, Alam MS, Nehdi M (2008) Experimental investigation on the seismic behavior of beam-column joints reinforced with superelastic shape memory alloys. J Earthq Eng 12(7):1205–1222

Zhang Y, Zhu S (2007) A shape memory alloy-based reusable hysteretic damper for seismic hazard mitigation. Smart Mater Struct 16(5):1603–1613

Zhang YF, Zhu SY (2008) Seismic response control of building structures with superelastic shape memory alloy wire dampers. J Eng Mech 134(3):240–251

Zhu S, Zhang Y (2007) Seismic behaviour of self-centring braced frame buildings with reusable hysteretic damping brace. Earthq Eng Struct D 36(10):1329–1346

Zhu SY, Zhang YF (2008) Seismic analysis of concentrically braced frame systems with self-centering friction damping braces. J Struct Eng 134(1):121–131